Bioactive Materials 23 (2023) 261–273

Contents lists available at ScienceDirect

Bioactive Materials

journal homepage: www.keaipublishing.com/en/journals/bioactive-materials

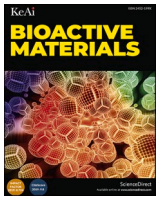

Biodegradable magnesium materials regulate ROS-RNS balance in pro-inflammatory macrophage environment

Maria P. Kwesiga [a], Amani A. Gillette [b,c], Fatemeh Razaviamri [a], Margaret E. Plank [a], Alexia L. Canull [a], Zachary Alesch [a], Weilue He [a], Bruce P. Lee [a], Roger J. Guillory II [a,*]

[a] Department of Biomedical Engineering, Michigan Technological University, Houghton, MI, USA
[b] Morgridge Institute for Research, Madison, WI, USA
[c] Department of Biomedical Engineering, University of Wisconsin-Madison, Madison, WI, USA

ARTICLE INFO

Keywords:
Biocorrosion
Macrophage activation
Nitroso-redox balance
Mg

ABSTRACT

The relationship between reactive oxygen and nitrogen species (ROS-RNS) secretion and the concomitant biocorrosion of degradable magnesium (Mg) materials is poorly understood. We found that Mg foils implanted short term in vivo (24 h) displayed large amounts of proinflammatory F4/80+/iNOS + macrophages at the interface. We sought to investigate the interplay between biodegrading Mg materials (98.6% Mg, AZ31 & AZ61) and macrophages (RAW 264.7) stimulated with lipopolysaccharide (RAW 264.7^{LPS}) to induce ROS-RNS secretion. To test how these proinflammatory ROS-RNS secreting cells interact with Mg corrosion in vitro, Mg and AZ61 discs were suspended approximately 2 mm above a monolayer of RAW 264.7 cells, either with or without LPS. The surfaces of both materials showed acute (24 h) changes when incubated in the proinflammatory RAW 264.7^{LPS} environment. Mg discs incubated with RAW 264.7^{LPS} macrophages showed greater corrosion pitting, while AZ61 showed morphological and elemental bulk product changes via scanning electron microscopy-energy dispersive X-ray spectroscopy (SEM-EDX). X-ray photoelectron spectroscopy (XPS) analysis showed a reduction in the Ca/P ratio of the surface products for AZ61 disc incubated with RAW 264.7^{LPS}, but not the Mg discs. Moreover, RAW 264.7^{LPS} macrophages were found to be more viable in the acute biodegradative environment generated by Mg materials, as demonstrated by calcein-AM and cleaved (active) caspase-3 staining (CC3). LPS stimulation caused an increase in ROS-RNS, and a decrease in antioxidant peroxidase activity. Mg and AZ61 were found to change this ROS-RNS balance, independently of physiological antioxidant mechanisms. The findings highlight the complexity of the cellular driven acute inflammatory responses to different biodegradable Mg, and how it can potentially affect performance of these materials.

1. Introduction

Ischemic heart disease is the leading cause of death and disability worldwide, affecting at least 126 million individuals [1]. The gold standard for treating patients is percutaneous coronary intervention (PCI) with a bare metal or drug eluting stent [2,3] which has limitations that include acute thrombotic events, hypersensitivity to the drug eluting polymer coating, neointima response from inflammatory reactions, and stent fracture [4,5]. The next generation of stents currently in consideration to address the majority of these limitations are biodegradable metal stents [6]. Magnesium (Mg), the most prominent biodegradable metal stent candidate, has gained popularity in the last decade because of its biocompatibility and potential to accelerate tissue repair as the metal degrades [7,8]. Extensive research has shown the safety, biocompatibility, corrosion profile and mechanical strength of Mg based materials in vitro and in vivo [7,9–13]. In fact, Mg based stents are currently in clinical studies with encouraging outcomes [14–17]. However, problems of inadequate degradation rate, lumen loss, and neointimal hyperplasia remain [6].

The implantation of any biomaterial is expected to evoke some degree of an inflammatory reaction. Given its ubiquity, it is surprising that the importance of the inflammatory reaction is often overlooked in biomedical research studies. Patients eligible for PCI commonly present with health conditions that predispose towards a suboptimal vascular

Peer review under responsibility of KeAi Communications Co., Ltd.
* Corresponding author.
E-mail address: rjguillo@mtu.edu (R.J. Guillory).

https://doi.org/10.1016/j.bioactmat.2022.10.017
Received 3 June 2022; Received in revised form 21 September 2022; Accepted 11 October 2022

response to the implanted device, which often leads to substantial remodeling and immune responses after stenting. In the presence of a foreign body, immune cells produce a vast number of reactive oxygen and nitrogen species (ROS & RNS, respectively) that alter the nitroso-redox balance.

Nitroso-redox balance is a key factor in regulating cardiovascular oxidative stress [18,19]. Macrophages are the primary regulators of nitroso-redox balance throughout the inflammatory process, and possess a high propensity to release these reactive species in the extracellular space when activated to a more proinflammatory phenotype [20]. The principal ROS species produced during inflammation is superoxide, which will decompose into more stable ROS species like hydrogen peroxide (H_2O_2) by reacting with the enzyme superoxide dismutase or proton ions in solution [19,21]. The balance of ROS species in biological fluids is complex, and can be influenced by other reactive species such as RNS. The generation of RNS species, such as, nitric oxide (NO) is known to interfere with this reaction to form peroxynitrite, leading to reduced H_2O_2 concentration [22]. Mg has been shown previously to exert bioactive effects on macrophages, which would ultimately affect fluidic ROS-RNS balance [10,23,24].

In the present study, we demonstrate the acute presence of a pro inflammatory macrophage phenotype at the interface of implanted biodegradable Mg (98.6% wt.) and AZ31 (96% Mg, 3% Al 1% Zn, wt.) materials in a subcutaneous in vivo mouse model. We propose a new in vitro method to study this acute inflammatory environment upon Mg contact by suspending a non-corroded mechanically polished disc of Mg (98.6%) and AZ61 (93.6% Mg, 5.62% Al, Zn 0.74%, 0.23% Mn, wt.) 2 mm above a monolayer of RAW 264.7 macrophages stimulated with 100 ng/mL of exogenously delivered lipopolysaccharide (RAW 264.7^{LPS}). The suspension of the disc via attachment to the cell culture lid, as opposed to direct cell culture on the metal surface, allows for three important parameter distinctions: 1. measurement of surface features and corrosion products that directly interact with the culture media and molecules actively produced from the cells, 2. spatial localization and analysis of cells close to and far from the degrading material and 3. assessment of cell viability and correlation of metabolic changes with the degrading metal, without any modifications to standard cell culture conditions. RAW 264.7^{LPS} cells are well known to increase RNS generation by upregulation of inducible nitric oxide synthase (iNOS), increase ROS production, and change the extracellular proteome by excreting inflammatory cytokines [25,26]. The corrosion of biodegradable materials induces cell death, damage and lysis that release damage associated molecular patterns (DAMPs) such as mitochondria and ATP, which in turn stimulate an inflammatory response in immune cells, such as macrophages [27]. In our model, we directly rely on the temporal secretion response of RAW 264.7^{LPS} cells to produce extracellular ROS-RNS conditions in the presence of Mg materials. We then describe the intricate interaction between the cells and two different degrading Mg metals, as well as the cellular changes that occur under LPS stimulation.

2. Materials and methods

2.1. In vivo implantation

Mg (98.6% wt.) foils approximately 0.3–0.5 mm thick (a donation from the Materials Sciences and Engineering department, Michigan Technological University, Houghton, MI, USA) and AZ31 foils (0.25 mm, product # MG01-FL-000150 Good Fellow Coraopolis, PA, USA) were used in the in vivo study. The materials were cut into approximately 4 × 8 mm pieces and sterilized by ethylene oxide before surgical implantation in the subcutaneous tissue on the ventral side of the abdominal wall in wild type C5BL/6 mice for 24 h. The same surgical manipulation was performed in the subcutaneous abdominal wall of mice without metal implants (Sham). After 24 h, subcutaneous tissue implants with and without metal materials were harvested, snap frozen in liquid nitrogen and stored at −80° Celsius (°C) prior to histological analysis. The animal study was approved by the Michigan Technological University Institutional Animal Care and Use Committee (IACUC) and in accordance with guidelines set by the Panel on Euthanasia of the American Veterinary Medical Association. Samples were cryo-sectioned onto VistaVison(™) histobond slides (VWR, USA). Cross sections were then fixed with a neutral buffered 10% formalin solution and stained with hematoxylin and eosin (H&E). Slides were imaged using a Zeiss Axioscan.Z1 automated slide scanner. Fluorescently stained sections were labeled against F4/80 (254036, US Biological, Salem, MA, USA) and iNOS (13120S, Cell Signaling Technology, USA) using a primary antibody 1:400 ratio following fixation and counterstained with DAPI. Secondary antibodies used were Alexa fluor 647 and Alexa fluor 488. The samples were then mounted with Fluoromount aqueous mounting medium (Millipore Sigma St. Louis, MO, USA) and imaged using a Zeiss Axioscan.Z1 automated slide scanner with appropriate excitation wavelengths and filters.

2.2. In vitro culture setup

We used an in vitro approach that suspends the disc made from the material of interest above the cultured cell monolayer, in either 6 well plates or 10 cm dishes. Mg (98.6%) and an aluminum bearing Mg alloy (AZ61–93.6% Mg, 5.62% Al, Zn 0.74%, 0.23% Mn, wt. Supplementary Table 1) rod (a donation from the Material Sciences department, Michigan Technological University) were machined down to 14 mm diameter and cut into 6.5 mm discs using a Buehler IsoMet 1000 precision saw. A 1.98 mm drill bit on a drill press and 3–48 plug tap were used to add a threaded hole to one side of the discs to a depth of approximately 3 mm. The other side was then mechanically wet polished using silicon carbide polishing paper at 600, 800, and 1200 grit in sequence on a Buehler EcoMet 3000 grinder-polisher. After the final polishing step, the discs had been reduced to approximately 6 mm in height and were dried by compressed air. Discs were then washed by ultrasonic bath in 100% ethanol for 5 min then allowed to dry at room temperature in a fume hood. Holes of approximately 2.38 mm in diameter were drilled into the center of polystyrene cell culture plate lids.

The discs were mounted to the lid using 11.11 mm long 3–48 plastic screws. Two hundred proof ethanol was added to the plate wells to visually confirm that the polished surface would be fully immersed in the intended volume of media. The ethanol was then removed and the devices stored in dry room-temperature conditions. The devices were sterilized with ethylene oxide or ultraviolet light prior to cell culture experiments. The chemical composition, diameter and thickness of the discs were measured before immersion in cell culture media (Supplementary Table 1 & Supplementary Fig. 1A&B). We were interested in the cellular response as well as changes to properties on the material surface. In order to accomplish this, two main culture configurations were used, a 6 well plate model and a 10 cm dish model. The details that summarize the culture configurations are presented in Table 1, below. The 6 well plate model was used for all cell viability and apoptosis assays. Following experiments, the discs used in this setup underwent x-ray spectroscopy (XPS) and scanning electron microscopy (SEM) analysis. The culture fluid was collected for elemental determination by inductively coupled plasma-optical emission spectrometry (ICP-OES). These analyses were chosen in order to investigate the equilibrium conditions of the cell monolayer, cell culture media, and the discs without a media renewal. The 10 cm dish configuration was used to investigate changes in nitroso-redox balance, which is heavily time dependent. Additionally, the larger dishes allow for greater cell culture media collection, which allows for more robust measurements for ROS-RNS. We also leveraged the larger amount of protein collected from the 10 cm dishes to assess iNOS and glutathione peroxidase 1 (GPX1) expression by Western blot analysis.

Table 1
Models and parameters assessed in the two experimental co-culture systems.

Parameters	6-well plate co culture	10 cm dish co-culture
Initial seeding density	1×10^5 (1.1×10^4/cm)	1.5×10^6 (2.6×10^4/cm)
Approximate cell # @ confluence	$>2 \times 10^5$	$>3 \times 10^6$
Cell culture media volume (mL)	4	15
Disc surface area (cm^2)	2.7	2.7
Surface Area/Volume (/cm)	0.7	0.2
Time endpoints (hour)	24	24, 72
Fluid replacement	None	Every 24 h
Analysis on discs	SEM, XPS	–
Analysis on culture media	ICP, pH	H_2O_2, peroxidase, NO_2^-/NO_3^-
Analysis on cells	Viability, apoptosis, elemental content	Western blot - GPX1, iNOS

2.3. Cell viability and apoptosis

The mouse macrophage cell line (RAW 264.7) was purchased from ATCC (Manassas, VA, USA). The cells used in experiments were thawed from cryopreservation at passage number 3–4 and cultured in DMEM media (high glucose 4500 mg/L), 10% fetal bovine serum and 1% penicillin streptomycin (culture media) at 37 °C and 5% CO_2. At passages 5–6, RAW 264.7 were subcultured onto 6 well plates at a seeding density of 1×10^5 cells per well. After 24 h, the culture media was changed, and the cells were stimulated with 100 ng/mL of LPS *Escherichia Coli* (Millipore Sigma). Cell cultures without discs were used as controls. The attached Mg and AZ61 discs were then immersed in the culture media, down from the lid to a position 2 mm above the cell monolayer. Approximately 40% of the disc was exposed to the culture media. The cells and discs were incubated together for 24 h. After 24 h of combined culture, a live-dead assay was carried out using 2 μM calcein-AM and 2 μg/mL ethidium bromide (Invitrogen Thermofisher, Waltham, MA, USA), which stain live and dead cells, respectively. Hoechst dye at 10 μg/mL (Thermofisher) was added to stain cell nuclei. The cells were incubated with the reagents in phosphate buffered saline (PBS) for 15 min in the dark at room temperature and imaged using an EVOS-FL Auto™ fluorescent microscope. For evaluation of cellular apoptosis, we used an antibody against cleaved (active) caspase-3 (CC3). Cells cultured for 24 h with Mg and AZ61 discs were washed 3 times in PBS and fixed at room temperature for 10 min with 4% formaldehyde fixative solution. The fixative solution was removed and the cells washed 3 times in PBS for 5 min each wash. The cells were then permeabilized with 0.1% Triton X-100 and blocked with 10% goat serum in 5% bovine serum albumin (BSA) solution for 30 min. The primary antibody (ab13847 Abcam, Cambridge, MA, USA) was added at 1:200 dilution and incubated for 1 h at room temperature. After 2 PBS washes, the secondary antibody (ab150077) at 1:500 dilution was added and incubated for another hour in the dark at room temperature. The cell monolayer was washed twice with PBS and 4′,6-diamidino-2-phenylindole (DAPI) solution (1 μg/mL) was added for 2 min. After 2 quick PBS washes, the cells were imaged using an EVOS-FL Auto™ fluorescent microscope.

2.4. Single cell analysis

For assessment of viability and CC3 activity in the cells, a semi-automated image analysis code was created using standard and customized modules within CellProfiler (v.4.0.7) [28]. First, the acquired nuclei (DAPI), dead cells (Texas Red), live cells and CC3 (GFP) images were loaded into CellProfiler. The GFP image was rescaled to have values between 0 and 1. The raw GFP image was multiplied by 100x the rescaled GFP image and the resulting image was smoothed using a Gaussian filter with an artifact diameter of 10. The smoothed GFP image was used to automatically identify the cells by using a propagation method with a global minimum cross-entropy thresholding strategy to prevent segmentation of the background. The DAPI image was used to identify the nuclei of the cells by a minimum cross-entropy global thresholding strategy with bounds of 0 and 1. For Texas Red, dead cells were automatically identified using the global robust background thresholding with a correction factor of 1.05. These objects were compared with DAPI to count the number of dead cells. The typical object diameter range for these images was 30–100, and the intensity was used to distinguish between clumped objects. All pipelines for each image category were followed with a manual step that allows the user to edit the cell masks as needed (Supplementary Fig. 2). Finally, the intensity was measured for each cell, masks of the cells were generated, and both were exported.

Histograms of number of cells vs. mean viability/CC3 intensity were generated for each condition and fitted to a Gaussians distribution mixture model as previously described [29]. Gaussian mixture distribution models were generated in MATLAB (version 2020b) using the equation [30]:

$$f(y;\Phi_g) = \sum_{i=1}^{g} \pi_i \varphi(y;\mu_i, V_i)$$

where g is the number of subpopulations, $\varphi(y;\mu_i, V_i)$ is the normal probability density function with mean μ_i, variance V_i, and π_i being the mixing proportion. Goodness of fit was calculated given a set of subpopulations (g = 1, 2, or 3) using an Akaike information criterion [31]. This process was repeated 100 times and only the model with the best fit was implemented after the number of subpopulations was determined based on the lowest Akaike score. For easy visual comparison, the distributions shown have been normalized to have an area under the curve of one (Supplementary Fig. 1E, F&G).

2.5. Nitroso-redox assays

The culture media collected at 24 and 72 h were assessed for H_2O_2. The H_2O_2 concentration was quantified using the Pierce™ Quantitative Peroxide Assay Kit (23280, Thermo Fisher Scientific, Waltham, MA, USA) which detects H_2O_2 based on Ferrous Oxidation-Xylenol orange (FOX). 20 μL of culture media and 200 μL of FOX assay working reagent were added to a black, clear bottom 96-well plate and incubated for 15 min at 25 °C. The absorbance was measured using a plate reader (Beckman Coulter DTX 880 Multimode Detector) at 595 nm. The measured absorbances were converted to molar concentration by referencing absorbances from the standard curve of 1–1000 μM H_2O_2 prepared from a fresh 30% H_2O_2 stock solution diluted in deionized water (Macron Fine Chemicals, USA). In order to evaluate exogenously released peroxidases, we adopted a luminol- H_2O_2 chemiluminescence system extensively applied in immunoblot detection [32]. In this reaction peroxidase catalyzes the oxidation of the substrate luminol which emits an optical signal, with H_2O_2 acting as the electron acceptor [33]. The protein quantity from culture media collected at 24 and 72 h was measured using the Bradford assay [34]. 100 μg/mL of protein was added to clear 96 well plates and an equal amount of ECL substrate (Bio-Rad, USA) was added to each well. The samples were incubated for 15 min prior to imaging using chemiluminescence detection with an Azure 600 imager and analyzed using ImageJ (Java 1.8, Supplementary Fig. 3). For RNS determination, culture media at 24 and 72 h was assessed using the Griess assay(Cayman chemical, Ann Arbor, MI, USA) which measures RNS in the culture media in a 2 step process that involves conversion all NO_3^- into NO_2^- followed by addition of a Griess reagent that reacts with NO_2^- to produce a purple azo compound that can be measured spectrophotometrically [35]. The protocol and analysis were determined using the manufacturer's instructions.

2.5.1. Glutathione peroxidase and iNOS detection

The cell monolayers were scraped, centrifuged, resuspended in 1 mL of RIPA lysis buffer (ThermoFisher scientific) containing ethylenediaminetetraacetic acid (EDTA) and protease cocktail inhibitor 1:100 dilution (ThermoFisher scientific) and kept on ice. The cell lysates were incubated for 30 min on ice with a plate shaker set at 180 revolutions per minute (RPM) and centrifuged at 12,000 RPM for 20 min at 4 °C. The supernatant was obtained and protein concentration was determined using the Bradford assay. An equal amount of loading buffer containing dithiothreitol 54 mg/mL (Bio-Rad) was added to each sample, boiled at 100 °C for 5 min and immediately placed on ice for 2 min. Approximately 15–20 μg of protein was loaded in a 10% SDS-PAGE gel and separated by electrophoresis at 100 V for approximately 90 min. The proteins were transferred to immobilon®-FL PVDF membrane (*LI-COR,* USA) using wet transfer blotting (Bio-Rad) with the current set at 135 mAmps for 90 min. The membrane was incubated in Odyssey blocking buffer (TBS) for 30 min to block nonspecific binding sites followed by incubation in TBS containing 0.2% of tween20 (TBS-T) and primary antibodies GPX1 (ab22604, ABCAM) at 1:1000 dilution, iNOS (PA3-030A, ThermoFisher scientific) at 1:2000 dilution overnight at 4 °C. Glyceraldehyde-3-Phosphate Dehydrogenase (GAPDH) (MCA4740, Bio-Rad) at 1:500 dilution and Coomassie stain (Bio-Rad) were used as housekeeping controls (Supplementary Fig. 4). The membrane was washed 4 times with TBS (0.1% tween20) and incubated in TBS-T with the secondary antibodies IRDye 680RD and 800CW (*LI-COR*) at 1:10,000 dilution for 1 h, then extensively washed in TBS (0.1% tween20), visualized with an Azure 600 imager and analyzed using ImageJ (Java 1.8).

2.6. Elemental analysis of culture media and cell monolayers

The cell monolayers were rinsed in DPBS and collected using a cell scraper and centrifuged for 5 min at 1000 RPM. The supernatant was removed and 1 mL of lysis buffer containing 1% Triton-X 100, 50 mM Tris, 100 mM sodium chloride (NaCl) and EDTA -free protease inhibitor in deionized water was added to the cell pellet. The mixture was transferred to 1.5 mL microcentrifuge tubes containing 1.4 mm diameter ceramic beads. A Bead Mill 4 Homogenizer (Fisher Scientific) was used to enhance cell lysis. The homogenizer was operated at a speed of 5 for 2 min, the vials were then placed on ice for 2 min and the cycle was repeated again for 2 min, with an additional 2 min on ice and finally 1 min again in the homogenizer and placed on ice for another minute. The samples were centrifuged for 5 min at 12,000 RPM and the supernatant transferred into 1.5 mL centrifuge tubes. Acid digestion was performed in 1% nitric acid for the cell lysate suspension as well as the culture media. All samples were stored at 4 °C overnight prior to measurements using a PerkinElmer Optima 7000DV instrument. Standards were made by diluting certified standards from Spex CertiPrep, PerkinElmer or Inorganic Ventures. An independent standard was analyzed to verify the calibration standards. Check standards were analyzed every 12 samples with recoveries of 100 ± 10%. Samples were diluted with water, if needed. A blank matrix solution was analyzed along with the samples to look for contamination and matrix interferences. The lowest calibration standard used was 0.01 mg/L and the limits of detection for elements analyzed are; Phosphorus (P): 0.03, Mg: 0.002, Calcium (Ca): 0.002, Manganese (Mn): 0.002, Iron (Fe):0.005,Copper (Cu): 0.06, Aluminum (Al): 0.05 mg/L. A Coomassie based protein detection method following gel electrophoresis of the samples was used to confirm similar protein content within the experimental groups (Supplementary Fig. 5). The culture media was collected and used to measure the Mg, Ca, and, P content.

2.7. pH measurements

The culture media was collected and the pH measured using an Orion™ ROSS™ Sure-Flow™ pH Electrode (Thermofisher, Waltham, MA, USA). All samples were placed in the incubator set at 37 °C, 5% CO_2 prior to measurements to avoid fluctuations in the pH readings.

2.8. Material characterization

After immersion in culture media, the discs were dried and imaged by scanning electron microscopy (Philips XL 40 ESEM). Select discs were embedded in epoxy and ground using a standard metallographic ascending grit series to obtain a cross sectional view, and coated with an (Ir) conductive substrate. Energy dispersive X-ray spectroscopy (EDS) maps were collected for each condition at an accelerating voltage of 15 kV and average deadtime of 10%–20%. X-ray photoelectron spectroscopy (XPS) characterization was carried out to determine the elemental composition of the Mg and AZ61 surfaces (Thermo Scientific ESCALAB 250xi). A survey spectrum was collected using a 900 μm × 900 μm spot size and a standard aluminum X-ray source from 0–1200 eV, with a step size of 1.00 eV and pass energy of 150 eV, to identify all elements present at the surface. Two experimental replicates were analyzed for both Mg and AZ61, with n = 3 spots per sample (total n = 6) taken for each experimental condition. Spectra were analyzed in CasaXPS, and were charge corrected to adventitious carbon at 248.8 eV. Elemental concentrations at the surface were determined with relative sensitivity factors provided in the CasaXPS "quantify" function and library.

2.9. Statistical analysis

The data was uploaded into Graphpad Prism (v9.3.0) for analysis. An unpaired Student's T-test with Welch's Correction for samples of unequal variance was used to test for statistical significance at *$p < 0.05$ and ****$p < 0.0001$. Differences in variables between multiple groups were tested using a one-way ANOVA, a Dunnett's multiple comparisons test with a single pooled variance was used to explore differences between multiple groups, with significance at #$p < 0.05$ and ####$p < 0.0001$.

A z-score heatmap was generated for each experiment using the equation:

$$z - score = \frac{(\mu_{condition} - \mu_{all})}{\sigma_{all}}$$

Where the mean of each individual condition is compared to the mean of all conditions combined within an experiment so that positive or negative correlations are in respect to the variable measured across the entire population.

3. Results

3.1. Acute in vivo localization of pro inflammatory macrophages near Mg materials

The acute inflammatory reaction is characterized by the recruitment of pro inflammatory macrophages expressing the iNOS protein that is well known to produce RNS species NO [36,37]. To localize the iNOS signal to macrophages, we also assessed the expression of the surface glycoprotein F4/80 that is uniformly expressed in macrophage cells [38]. A mild inflammatory response was observed in the sham controls with few cells staining positive for iNOS and F4/80 in the area surrounding the subcutaneous pouch (Fig. 1. A, B &C). The explants with both Mg foils showed a marked increase in cells expressing iNOS and F4/80 around the implant as well as areas further away from the site of implantation (Fig. 1. E, F&G). AZ31 also followed a similar trend (Fig. I, J&K). H&E of these sections also showed minimal cell recruitment and reduced extracellular matrix formation in sham compared to Mg and AZ31. Interestingly, AZ31 also showed possible signs of necrosis at the interface of the material and the surrounding tissue. These observations indicate Mg implants caused a local inflammatory environment

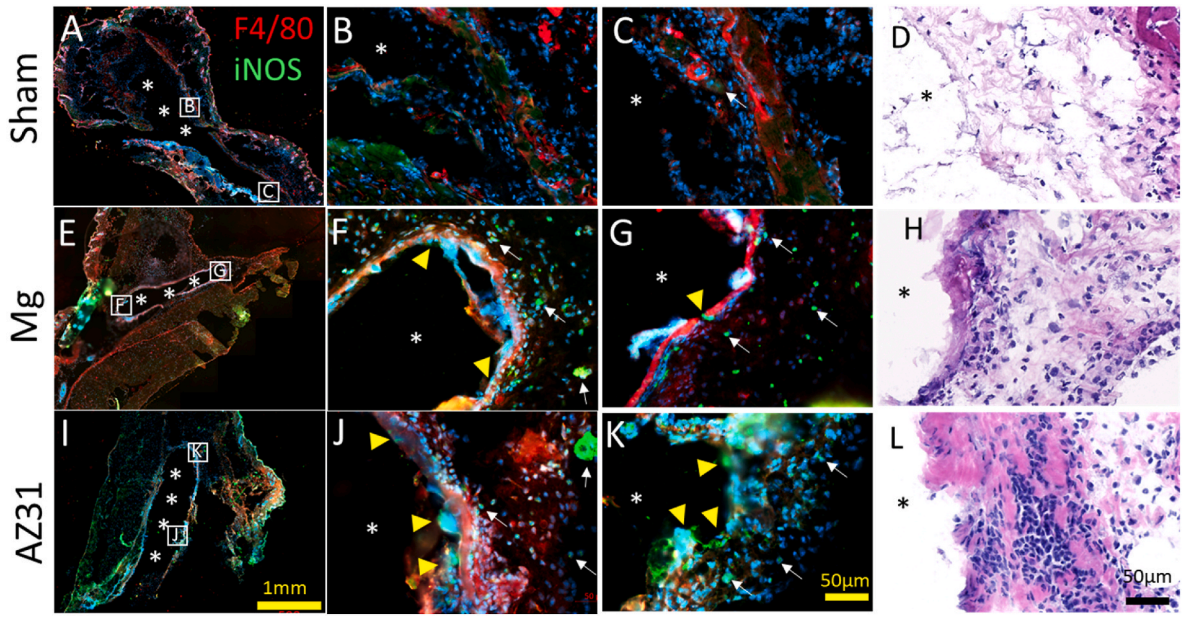

Fig. 1. Pro-inflammatory macrophages are present near Mg and AZ31 at 24 hrs subcutaneously A, **E**, and **I** show macroscopic view of tissue sections with either a sham procedure performed (**A**), Mg foil implanted (**E**), or AZ31 foil implanted (**I**). **B** and **C** are magnified views from boxed regions in panel **A**. **F** and **G** are magnified views from panel **E**. **J** and **K** are magnified views from panel **I.** Panels **D**, **H**, and **L** are H&E stains from representative areas of the material interface with the corresponding row. White or black "*" denotes where the material was implanted, showing tissue directly at the interface.

mediated by pro-inflammatory macrophages. To further investigate the detailed cellular and chemical mechanisms, we placed Mg materials in an in vitro macrophage culturing system that allows for easier variable control.

3.2. *RAW 264.7^{LPS} cells modulate bulk Mg corrosion products in a material dependent manner*

We incubated the Mg and AZ61 discs in the 6 well plate configuration for 24 h, with and without LPS stimulated RAW 264.7 cells. After 24 h of the disc culture with RAW 264.7 and RAW 264.7^{LPS} cells, distinct surface features are apparent for both Mg and AZ61. Lighter colored corrosion products were present for Mg + RAW264.7 compared to Mg + RAW 264.7^{LPS}. Interestingly, this trend is reversed for AZ61 + RAW 264.7 and AZ61 + RAW 264.7^{LPS} (Supplementary Fig. 6). We found a continuous corrosion film on Mg + RAW264.7 and AZ61 + RAW264.7, with thicknesses of 3.5 ± 1.1 μm and 6.2 ± 0.9 μm respectively. Upon LPS treatment, presentation of the bulk films for both materials were altered. Fig. 2A demonstrates representative changes seen after LPS stimulation for the two materials. Pitting style corrosion was seen for Mg and was highly variable, depicted in Fig. 2A. For the AZ61+ RAW 264.7^{LPS} group, a densification of the bulk corrosion film has occurred, with an average thickness of 3.3 ± 1.3 μm. Areas of granular dense corrosion product can be seen throughout, which largely dominates the corrosion product.

Further assessment of the bulk product with SEM-EDS on discs that were epoxy embedded and polished on the cross-sectional axis shows that a corrosion film primarily consisting of magnesium (Mg), phosphorous (P), calcium (Ca), oxygen (O), chlorine (Cl), sodium (Na) and carbon (C) was present on Mg discs (Fig. 2B). For the AZ61 discs, detected elements within the bulk products were mainly Mg, P, Ca, O, Cl, Na, C, zinc (Zn), and aluminum (Al). Largely, no discernible difference in the elemental composition of the bulk product for Mg + RAW264.7 and Mg + RAW 264.7^{LPS} exists, which can be seen by three representative EDS sites for each condition in Fig. 2B&C. However, there were differences between the composition of the bulk products between AZ61 + RAW264.7 and AZ61 + RAW 264.7^{LPS} (Fig. 2D&E). These differences manifest as increased presence of Al and Zn within the corrosion product for AZ61+ RAW 264.7^{LPS}. Additionally, the products contain more Ca and P (Fig. 2E). AZ61 + RAW 264.7^{LPS} discs also possessed a large amount of granular corrosion products, which mostly consisted of C, O, and Mg (Fig. 2E, sites 4&5). This granular product is strikingly different when compared to AZ61 + RAW 264.7, which shows a homogenous film consisting of P, Ca, O, and Mg. It should be noted that the appearance of manganese (Mn) particles in the AZ61 + RAW 264.7 condition are due to occurrence in the alloy [39]. Fig. 2F&G show distribution of the elements within the bulk film via EDS mapping.

3.3. *RAW 264.7^{LPS} cells alter the surface chemistry of Mg materials*

Then, we evaluated discs cultured with RAW 264.7 and RAW 264.7^{LPS} cells *via* XPS. We selected XPS due to its inherent surface sensitivity and quantifiability [40,41]. For elemental quantification of the total survey scans, O1s, C1s, N1s, P2p, and Ca2p regions were used. High resolution N1s and O1s peaks were evaluated for binding energy shifts, but no differences were detected in the data. Overall, for the two conditions, Mg discs possess a higher atomic percentage (at%) of Ca and P on the surface (Fig. 3A) vs (Fig. 3B). For AZ61, the total amount of Ca and P increased when exposed to RAW 264.7^{LPS} (Fig. 3C&D). The at% increase was coupled to a decrease in the Ca/P ratio ($p < 0.001$, Fig. 3E). This decrease in ratio alludes to a stoichiometric change in the protective Ca/P film that forms during corrosion, which ultimately suggests that the RAW 264.7^{LPS} modulation of the fluid environment has altered the surface film that forms on the AZ61 material. Due to the overwhelming complexity of the immersion fluid, high resolution C1s, O1s, P2p, and Ca2p peaks were not fitted for chemical species.

Analyzing the pH of the culture media in the no metal control conditions shows a decrease in the pH once RAW 264.7 are cultured for 24 h (Supplementary Table 2 & Fig. 3F). Additionally, there is no change in the pH of the RAW 264.7^{LPS} compared to RAW 264.7 at 24 h. The pH values increased significantly upon culture with Mg and AZ61, with the highest culture media pH increase provided by Mg at 24 h. The pH values of the culture media exposed to Mg and AZ61 showed no apparent changes between RAW 264.7 and RAW 264.7^{LPS} conditions.

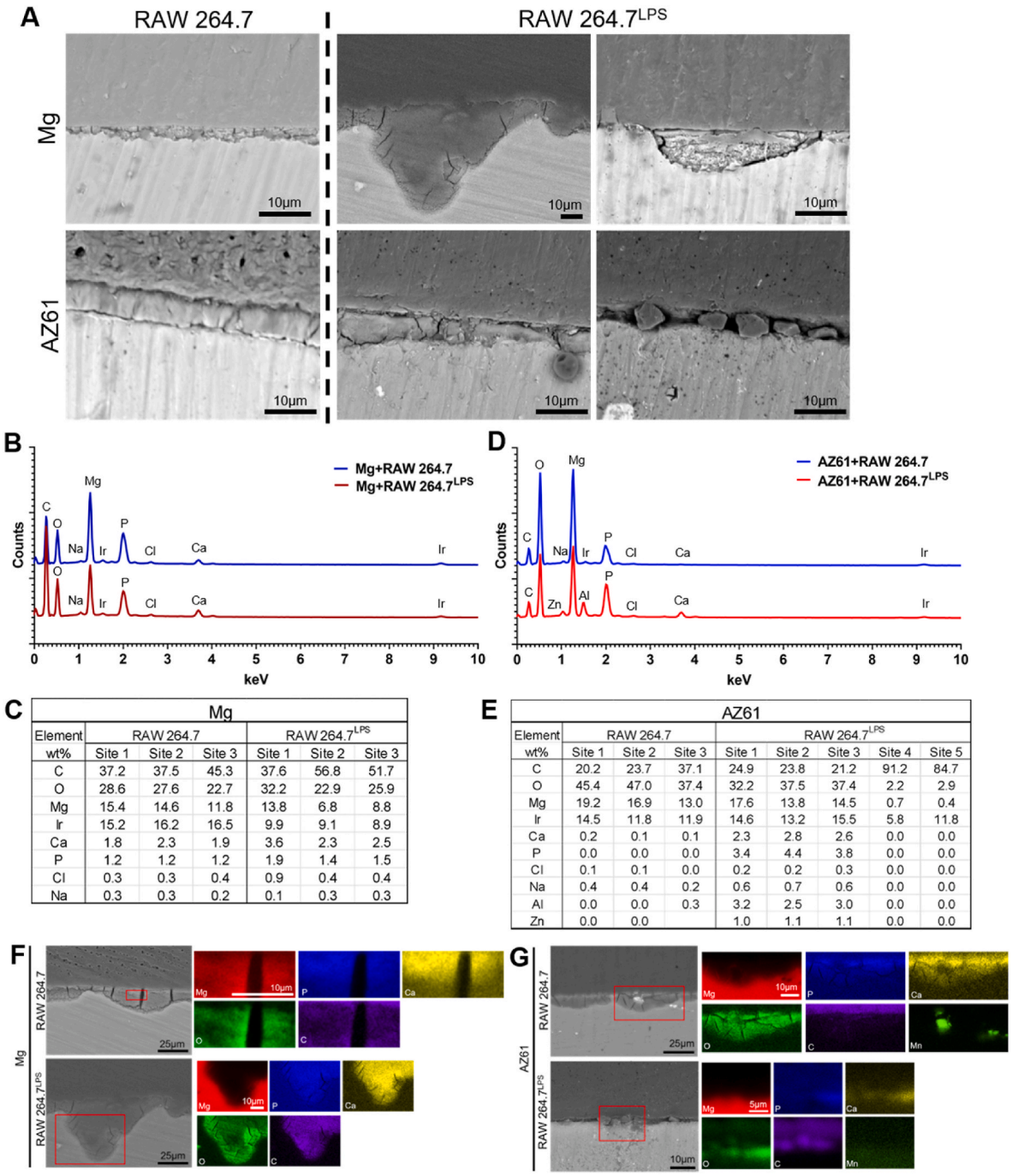

Fig. 2. Pro-Inflammatory conditions promote changes in bulk corrosion products. A presents SEM photomicrograph images showing morphological differences in the bulk corrosion products of Mg and AZ61 in the RAW 264.7 and RAW 264.7^{LPS} cell groups. **B&D** Representative EDS analysis on epoxy embedded and polished metal discs in the cross-sectional profiles for Mg and AZ61 respectively. **C&E** Summary of quantitative EDS analysis on multiple sites for each experimental condition. **F&G** EDS mapping of corrosion products performed for both incubated conditions of Mg and AZ61.

3.4. RAW 264.7^{LPS} viability response towards Mg corrosion

We intended to determine how Mg materials influence macrophage viability in our system, and employed a calcein-AM/ethidium bromide live-dead stain for the viability analysis. Interestingly, when we quantified the percentage of live cells, we saw no statistical changes in cell viability (Fig. 4A&B & Supplementary Table 3). For all groups there was a significant decrease in overall live cell number upon stimulation with LPS (Supplementary Fig. 1C). We then evaluated the progression of apoptosis since degradation products of Mg have been reported to be toxic to cells [11], by staining the RAW 264.7 cells exposed to the two material conditions for CC3 (Supplementary Table 3 & Fig. 4C).

Quantifying the CC3 intensity on a per cell level indicates that there is a reduction in CC3 intensity in Mg + RAW 264.7^{LPS} and AZ61 + RAW 264.7^{LPS} (Fig. 4D). Overall, there is a reduction in CC3 intensity for AZ61 cell culture when compared to Mg cell culture, likely due to the reduced corrosion of AZ61. Furthermore, there is a decrease in CC3 intensity between the unstimulated (RAW 264.7) and RAW 264.7^{LPS} for both materials ($p < 0.0001$). We then explored the relationship of cellular viability via CC3 intensity of total cells that were spatially located either directly underneath the disc or not directly underneath (Fig. 4E; close vs. far). Unexpectedly, live cells directly underneath the

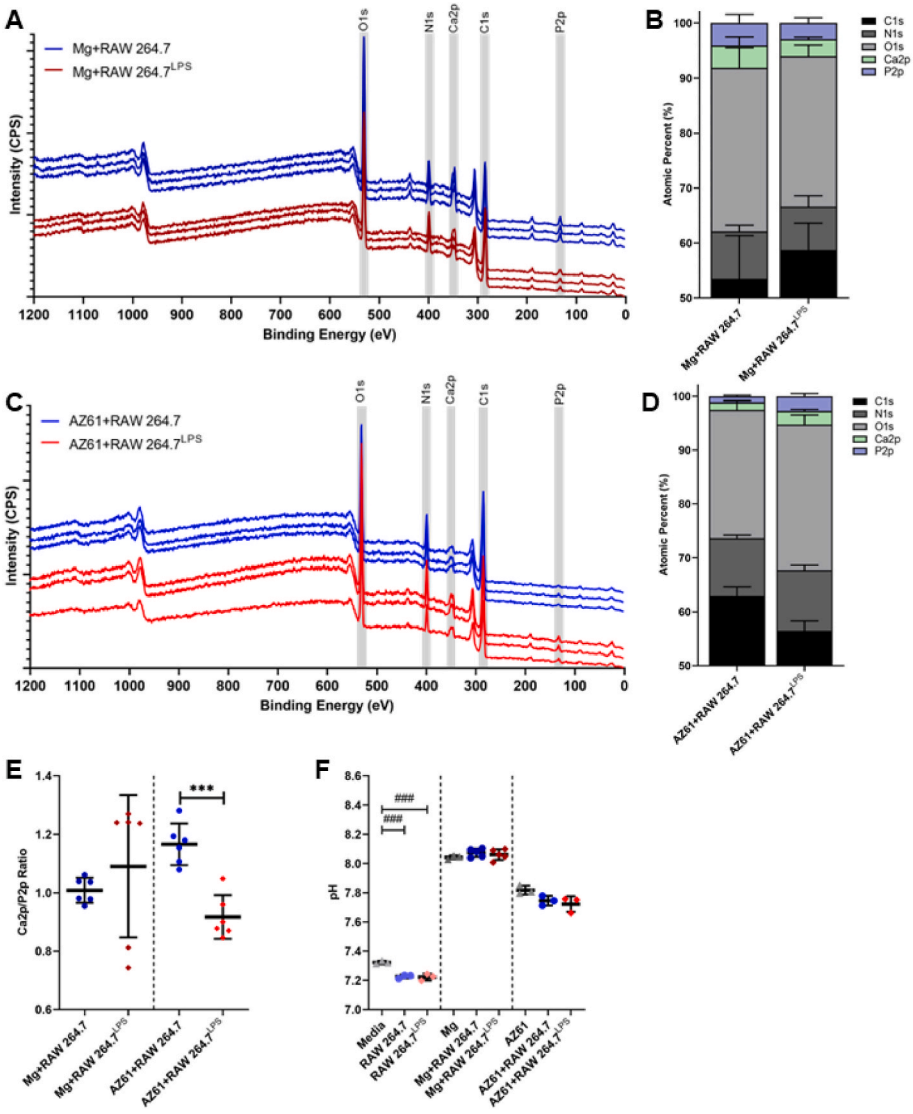

Fig. 3. XPS surface analysis of Mg and AZ61 discs cultured with RAW 264.7 in the absence and presence of LPS stimulation. **A** and **B** demonstrate the changes determined at% for Mg discs in RAW 264.7 and RAW 264.7^{LPS} cell groups. **C** and **D** show the changes in at% for AZ61 in RAW 264.7 and RAW 264.7^{LPS} cell groups. The Ca and P ratio of Mg and AZ61 discs (n = 6) is represented in **E.** The pH changes of culture media with no cells, controls (n = 3), Mg (n = 5) and AZ61 (n = 3) cultured with RAW 264.7 and RAW 264.7^{LPS} is presented in **F**. Unpaired Student's t-test ***p < 0.001; one-way ANOVA ###p < 0.001.

degrading material in Mg + RAW 264.7^{LPS} and AZ61 + RAW 264.7^{LPS} display a highly significant reduction in CC3 ($p < 0.001$). This data indicates that the proinflammatory LPS stimulation of RAW 264.7 cells may help increase viability in the presence of Mg corrosion.

Mg ion concentration has been shown to be a key factor that influences cell viability [11]. Therefore, we assessed the elemental Mg concentration within cells (intracellular) at 24 h using ICP-OES (Supplementary Table 2 & Fig. 4F). It is clear that there is higher intracellular Mg content when macrophages are cultured in the presence of either Mg or AZ61 (Fig. 4F). However, Mg causes a higher amount of intracellular Mg compared to AZ61. The intracellular Mg content for both RAW 264.7^{LPS} groups is reduced compared to RAW 264.7 counterparts ($p < 0.01$, Fig. 4F). No substantial changes in intracellular Ca or P were observed (Supplementary Fig. 7).

3.5. The degrading Mg and AZ61 discs influences ROS-RNS balance generated by RAW 264.7 and RAW 264.7^{LPS}

The nitroso-redox balance is the primary concern in aggravated inflammatory conditions. Enzymes such as peroxidases are a key player in modulating ROS species (H_2O_2) levels [19]. Therefore, we assessed ROS-RNS balance and peroxidase activity at 24 and 72 h in 10 cm dishes to accommodate for more robust measurements (Supplementary Table 4 and Fig. 5). The measurement of total peroxidase activity within the culture media at 24 h indicates that there is a decrease in total peroxidase activity for RAW 264.7^{LPS} compared to RAW 264.7 in the control group (Fig. 5A). A similar trend is observed for Mg and AZ61 cell cultures.

When H_2O_2 presence was measured via the Ferrous Oxidation-Xylenol orange (FOX) assay for RAW 264.7 and RAW 264.7^{LPS} cells cultured in control, Mg and AZ61 conditions at 24 h, we found an H_2O_2 concentration increase in RAW 264.7^{LPS} in the control group (Fig. 5B). A marked decrease is observed in Mg + RAW 264.7^{LPS} compared to Mg + RAW 264.7 ($p < 0.0001$). We interpret this as Mg corrosion causing an overall reduction in H_2O_2 generation of RAW 264.7^{LPS} cells. A non-significant decrease is also observed for AZ61 + RAW 264.7^{LPS} compared to AZ61 + RAW 264.7. The overall decrease is notable when compared to Mg groups. A Griess assay was used to assess RNS in controls, Mg + RAW 264.7, Mg + RAW 264.7^{LPS}, AZ61 + RAW 264.7 and AZ61 + RAW 264.7^{LPS} (Fig. 5C). The results show that Mg + RAW 264.7 and AZ61 + RAW 264.7 at 24 h were the only conditions that could initiate RNS production without LPS stimulation. LPS stimulation of all groups was potent in producing RNS, with the highest levels in AZ61 + RAW 264.7^{LPS} compared to Mg + RAW 264.7^{LPS} and control.

At 72 h, there is no apparent change in peroxidase activity for AZ61 + RAW 264.7 and AZ61 + RAW 264.7^{LPS} (Fig. 5D). The H_2O_2

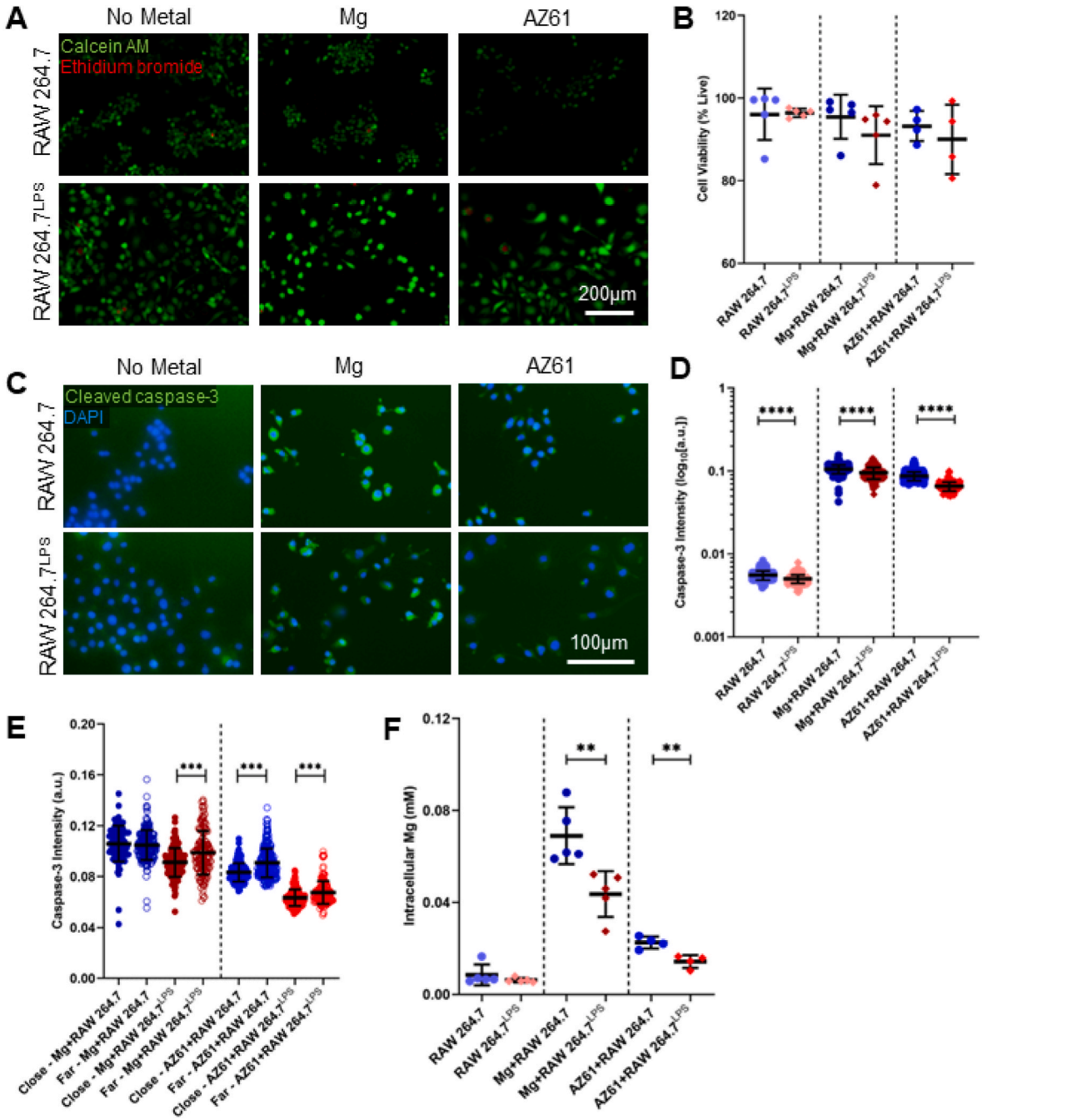

Fig. 4. RAW 264.7 cellular responses towards degradable Mg and AZ61 in unstimulated and LPS stimulated inflammatory conditions. A Representative images of cell viability of RAW 264.7 and RAW 264.7^{LPS} cultured with Mg and AZ61 stained for live (calcein-AM; green) and dead (ethidium bromide; red) markers. **B** Quantified cell viability percentage based on calcein-AM stain (n = 5 for Mg and n = 4 for AZ61). **C** Representative images stained for CC3, and **D** Quantified intensity of CC3 (n = 1510, n = 699, n = 300, n = 286, n = 498, n = 299 cells per group). **E**, Quantifying the CC3 levels based on their spatial location, close and far from the discs. **F** Intracellular Mg concentrations measured by ICP-OES for all experimental groups. Unpaired Student's t-test *p < 0.05, **p < 0.01, ***p < 0.001 and ****p < 0.0001.

concentration at 72 h trends are strikingly different for the two materials (Fig. 5E). For Mg, H_2O_2 concentrations are reduced when compared to the cell cultures at 24 h for unstimulated and stimulated cell cultures. The opposite trend is realized for the AZ61. Overall, there is an increase in the H_2O_2 concentration at 72 h for the AZ61 cell cultures when compared to 24 h for unstimulated and stimulated cell cultures. At 72 h, all groups showed no RNS without stimulation except for a very slight detection in AZ61 + RAW 264.7 (Fig. 5F). Mg + RAW 264.7^{LPS} showed the highest levels of RNS. AZ61 + RAW 264.7^{LPS} displayed an overall reduction in RNS levels from 24 to 72 h. This notable decrease in RNS for AZ61 + RAW 264.7^{LPS} at 72 h is concomitant with the appreciable increase of H_2O_2 at 72 h for the same group (Fig. 5E). These results indicate a time dependent modulation of nitroso-redox balance that is clearly demonstrated in AZ61 + RAW 264.7^{LPS}. It should be noted that these are not accumulated values, and the culture media was replaced every 24 h in order to maintain nutrient supply and facilitate the progression of corrosion in the culture environment.

We analyzed the cell lysate at 72 h with Western blot analysis for glutathione peroxidase 1 (GPX1). GPX1 is known for its detoxification properties against H_2O_2 and lipid hydroperoxides [42]. Upon

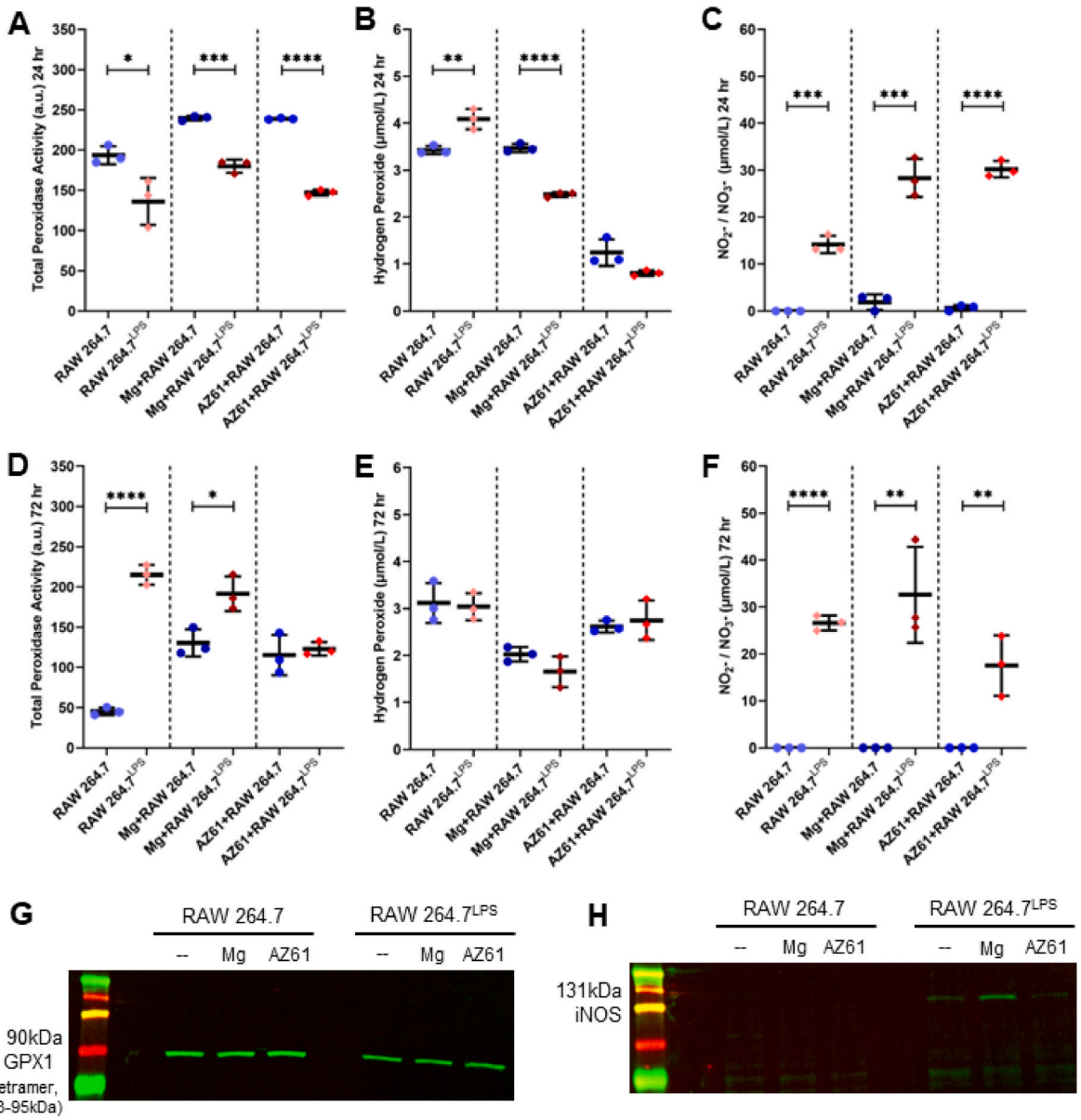

Fig. 5. pH and nitroso-redox balance changes observed in the presence of degrading Mg and AZ61 in RAW 264.7 and RAW 264.7^{LPS}. A represents total peroxidase activity, **B,** H_2O_2 and **C,** nitrite/nitrate levels at 24 h (hr), **D** represents total peroxidase activity **E,** H_2O_2 and **F,** nitrite/nitrate levels at 72 h (hr). For all groups, n = 3. **G,H** represents GPX1 and iNOS expression by Western blot analysis after 72 h (n = 2). Unpaired Student's t-test *p < 0.05, **p < 0.01, ***p < 0.001, ****p < 0.0001.

stimulation with LPS, all experimental cell culture groups experienced a decrease in GPX1 activity compared with their respective non-stimulated controls (Fig. 5G). There was no correlation with H_2O_2 concentrations in the culture media. This demonstrates that GPX1 is not a critical peroxidase enzyme in the presence of the degrading Mg and AZ61 materials. The cell lysates were also analyzed at 72 h by Western blot for inducible nitric oxide synthase (iNOS) upregulation, which is principally responsible for the production of RNS species NO which oxidizes into NO_2^-/NO_3^- in RAW 264.7^{LPS}. There was no detectable iNOS expression in unstimulated cultures. The highest iNOS expression is clearly seen in Mg + RAW 264.7^{LPS}, which correlates with increased RNS in the same group at 72 h (Fig. 5H).

4. Discussion

4.1. Acute in vivo macrophage environment

A key question regarding the validity of our in vitro model is whether proinflammatory macrophages are acutely present (24hr) near the interface of biodegrading Mg materials in vivo, and if their activation state can alter the ROS-RNS balance. We implanted Mg (98.6% wt.) and an aluminum bearing AZ31 alloy as foils into the subcutaneous space of C57BL/6 mice for 24 h, in order to visualize acute cellular recruitment (Fig. 1). We found that at 24hr in the Mg and AZ31 foils conditions, significant cell numbers were recruited near the interface, and these cells were predominantly F4/80+ macrophages. Additionally, macrophages near and away from the interface were iNOS+. iNOS is highly expressed by pro-inflammatory M1 macrophages, and is capable of synthesizing large amounts of NO. The presence of iNOS + macrophages in the sham condition was sparse within the pouch. This demonstrates

that the action of implanting a biodegradable Mg material for only 24hr will initiate an acute robust M1 response, and elevated ROS-RNS secretion. Toxicity was also seen via the H&E staining. Areas of apparent necrosis were present near the interface of both materials. Due to this toxicity, macrophages will increase their phagocytic ability and be stimulated towards a more pro-inflammatory phenotype. Although in vitro studies have shown an anti-inflammatory effect of Mg based salts and Mg material extracts on activated macrophages [10,23,43,44], the acute injury and toxicity caused by degrading Mg materials themselves will initiate a proinflammatory response that will outpace any acute anti-inflammatory benefits. This acute pro-inflammatory environment around the implant, which is characterized by ROS-RNS secreting macrophages, motivated us to study this cell-material interplay in greater detail using a novel in vitro model.

4.2. Proinflammatory RAW 264.7^{LPS} cells influence initial degradation on Mg based materials

The discs incubated with the LPS stimulated and unstimulated macrophages were evaluated for changes in their initial bulk corrosion films. When cross sections were made of the discs in order to evaluate the bulk product in greater detail, discrete changes were noted for the RAW 264.7^{LPS} incubated discs. Mg discs appeared to switch from homogenous to a more localized corrosion mode, displaying distinct pits for the RAW 264.7^{LPS} condition. This increase in corrosion attack was not accompanied by a significant change in the composition of the corrosion products, as seen by SEM-EDS in Fig. 2 B&C. Liu et al. found that when pure Mg is incubated with H_2O_2 in PBS, distinct changes in its corrosion susceptibility were seen with electrochemical impedance spectroscopy measurements, although it did not manifest as long term changes in Mg corrosion rate [45]. The change from homogenous to more localized corrosion when Mg incubated RAW 264.7^{LPS} mirrors the initial change in corrosion film susceptibility observed by Liu et al., although confirmation of whether this will accelerate long term corrosion rate remains to be determined.

Brooks et al. found that when AZ91 was incubated in a physiological solution containing supplemented H_2O_2, corrosion rate of the alloy over long immersion times increased [46]. They also found that an increase of Zn and Al within the corrosion media of the inflammatory fluid after 3 days of corrosion. While we did not detect Al or Zn in the culture fluid (likely due to concentrations below detection limits), we did observe an increase in the presence of these alloying elements within the corrosion layer in the RAW 264.7^{LPS} incubated AZ61 discs. This suggests that the corrosion of AZ61 discs incubated with RAW 264.7^{LPS} macrophages is more progressed when compared to the unstimulated condition. The product was also characterized by a consistently presenting granular deposit high in C, and contained O and Mg, which could represent an increased deposition of $MgCO_3$ in the LPS stimulated condition [47].

Overall, the AZ61 discs possessed much less surface Ca and P when compared to Mg (Fig. 3). This could allude to more corrosion progression taking place in general for the Mg discs and would correlate with the overall higher amount of Mg^{2+} in solution for both Mg culture conditions (Supplementary Fig. 7A). Although there was less Ca and P on the surface of AZ61 discs, the Ca/P ratio between AZ61 +RAW 264.7 and AZ61 +RAW 264.7^{LPS} were significantly different (Fig. 3). No statistical differences in the Ca/P ratio were observed for Mg. Wagner et al. has reported Ca/P ratios for immersed Mg materials in culture media with the addition of fetal calf serum [48]. They found that adding proteins to the solution hindered the formation of calcium phosphate layers over time, shown by linear decrease in Ca/P ratios via XPS analysis of the incubated discs. The expected Ca/P ratio for hydroxyapatite (HA) would be 1.67, derived from the formula $Ca_5(PO_4)_3OH$. Our Ca/P ratios for both conditions are near 1, and could be the result of either amorphous calcium phosphate, substitution of Ca with Mg, or a mixture of the two [48]. RAW 264.7^{LPS} cells cultured with AZ61 discs significantly reduced the Ca/P ratio lower than 1 (0.92 ± 0.08), which could indicate a decrease in the progression of stabilized HA phases for this condition. Ultimately, for AZ61, it could be concluded that the pro-inflammatory RAW 264.7^{LPS} cells may reduce the ability of the surface to form stabilized HA phases, which could potentially increase susceptibility towards degradation. Although this trend was not statistically observed for the Mg surface, large variation in the Ca/P ratio was observed for the Mg surface cultured with RAW 264.7^{LPS} cells. This demonstrates that the proinflammatory condition contributes towards destabilization of uniform passivating phases formed on Mg, which could potentially change the materials resistance to corrosion and is consistent with what has been seen for Mg in inflammatory conditions [45].

4.3. RAW 264.7 cell cytotoxicity response to degrading AZ61 and Mg while stimulated with LPS

We initially hypothesized that incubation of cells with the degrading Mg discs would generate cytotoxicity, partly due to the large increase in fluidic Mg^{2+}. Indeed, RAW 264.7 and RAW 264.7^{LPS} show a decreasing trend in viability in the 20–100 mM magnesium chloride salt solution range that we tested (Supplementary Fig. 1D). We would therefore expect the excess of 30 mM Mg (produced by the degrading Mg disc) to induce cell death (Supplementary Fig. 7A). We tested whether RAW 264.7 cells would experience cell death in the presence of Mg based materials and LPS stimulation. A live dead stain showed no significant changes in viability for RAW 264.7 and RAW 264.7^{LPS} cultured with the Mg and AZ61 materials. We saw morphological changes in the cultured cells for all groups, which would allude to cytotoxicity (Supplementary Fig. 8). Therefore, we used CC3 in order to evaluate apoptosis progression in the cultured cells incubated with Mg based materials. CC3 is an executioner caspase that upon cleavage and multimerization executes cell death in an irreversible manner and therefore, its presence is directly related to death induction timing [49].

We found that Mg + RAW 264.7^{LPS} CC3 intensity is significantly reduced and the effect is more pronounced with AZ61 +RAW 264.7^{LPS}. Furthermore, there is a spatial relationship with CC3 intensity in the cells relative to the material. RAW 264.7 cells that are further away from the degrading disc are more susceptible to cell death. In contrast, the RAW 264.7^{LPS} cells that are closest to the disc showed less CC3 based cell death. This result could help explain the biocompatibility response towards degrading Mg based materials in vivo. Viable cells are routinely seen near the interface of the material and are generally perceived to be inflammatory cells [50,51]. The cells that we see in Fig. 1 experience differential toxicity; some cells near the interface are dead/dying while others appear viable. In contrast to the in vivo observations, the majority of cell culture studies conclude that the degrading Mg environment is hostile, and produces cell death when materials are placed in close proximity to cells [11,52]. This suggests that factors such as inflammatory stimulation in Mg material degrading microenvironment enhance cell viability. Further studies such as cell subtyping and molecular mechanisms which include activation of transcription factor IKK/NF-κβ and downstream production of anti-apoptotic protein BCL 2 should be performed to better explain immune cell survival in degrading Mg materials [53,54].

The intracellular Mg concentration was dramatically reduced in RAW 264.7^{LPS} cultured in the presence of the two Mg based materials (Fig. 4F). Intracellular Mg influx and efflux is regulated by membrane channels whose expression can be modulated by the external Mg concentration [11,55]. Wang et al. [11]showed that increased Mg ion concentration in the culture media activated these channels in osteoblasts. Mg membrane channels that accommodate efflux of Mg ions can be activated and this is dependent on ATP and Mg ion concentration [55]. It is conceivable that inflammatory ligand stimulation that causes an increase in metabolic state in cells combined with the increase in overall extracellular Mg derived from the material exerts a heightened expression of these transporters, effectively reducing the intracellular Mg concentration and protecting cells from the death cascade. Further

studies would need to be assessed to explain this hypothesis and its role in immune cell survivability.

4.4. The ROS-RNS balance in stimulated RAW264.7 cells incubated with AZ61 and Mg

Several studies have shown that ROS can influence Mg corrosion. Bordbar et al. [56] found that simulated inflammatory conditions (150 mM H_2O_2 in phosphate buffered saline pH 5.5, without cells) accelerated corrosion of Mg alloy AZ91 compared to normal physiological media (phosphate buffered saline pH 7.4). Zhang et al. [24] studied RAW 264.7 macrophages seeded directly onto a Mg–Nd–Zn–based alloy (JDBM) surface for 72 and 168 h. The authors found that increased macrophage seeding density directly correlated to the corrosion rate of the JBDM alloy, which was attributed in large part to the intracellular ROS generation of RAW 264.7 cells which was found to be dramatically increased in the presence of Mg. In contrast Jin et. Al reports JDBM corrosion products and Mg salt solutions inhibit LPS induced THP macrophages production of intracellular ROS species [23]. The contradicting in vitro findings in these studies allude to a more complex interaction of the degrading material in biological microenvironments. RNS is a key player in maintaining redox balance during inflammation [19,22]. In fact, Mg materials have been shown to increase the expression of NOS enzymes that generate the RNS species NO [57]. Therefore, we assessed ROS and RNS levels in RAW 264.7 and RAW 264.7^{LPS} macrophage cultures in the presence of degrading Mg based materials. The ROS species H_2O_2 was reduced in LPS activated macrophage cultures incubated with the Mg materials compared to the control. This finding supports the anti-inflammatory effect of Mg based materials on macrophages [10,23,43,44]. However, a contradictory relationship exists between the two materials. At 24 h there is a much greater decrease in H_2O_2 in AZ61 compared to Mg in RAW 264.7^{LPS} culture media, the inverse is observed at 72 h incubation. It would be expected that AZ61 would have higher H_2O_2 levels than Mg, due to the large comparative reduction of Mg^{2+} in the culture media (Supplementary Fig. 7A). Our results suggest that other mechanisms of H_2O_2 scavenging could have occurred at the surface of the AZ61 material during the initial degradation process. Of interest, is that Mg materials incubated with RAW 264.7^{LPS} cells produced more RNS species when compared to the control. This is intriguing, as it followed an inverse trend with H_2O_2 production. Specifically, the concomitant increase in H_2O_2 in AZ61 + RAW 264.7^{LPS} at 72hrs corresponded with a decrease in RNS at the same time point. We further assessed peroxidase activity because of their critical role in maintaining ROS balance by using H_2O_2 as a co-substrate to oxidize organic and inorganic compounds [58]. Peroxidase activity was reduced with LPS stimulation for all experimental groups at 24 h. Moreover, the peroxidase enzyme GPX1 also showed no apparent changes in the presence of the degrading materials (Fig. 5G), which suggests that Mg based materials regulate nitroso-redox balance independent of physiological antioxidant mechanisms. To our knowledge, this is the first investigation to show how different degrading Mg materials affect nitroso redox balance. Our work highlights a role of RNS species in the acute degradation of Mg based materials in inflammatory microenvironments that needs to be explored.

In summary, we provide a Z-score analysis (Fig. 6A) with respect to the degrading Mg based materials incubated with RAW 264.7 and RAW 264.7^{LPS}. It should be noted that the rows of each experimentally measured variable are all included within the population mean, so that positive or negative correlations are in respect to the variable measured across the entire population. It is clearly seen that for both Mg and AZ61 materials, there is a reduction in relative CC3 intensity of RAW 264.7^{LPS}. This shows that the cells that remain during Mg degradation are apoptosis averse and consequently more metabolically active in both materials. We see that Mg, regardless of stimulation state or culture conditions causes a higher pH shift. In contrast, there is a mild decrease in pH values against the population mean for the AZ61 material. This finding demonstrates that Mg alkalizes the fluid compartment, regardless of the biological cellular influence. While AZ61 exerts a more moderate physiological response to the biological environment. This demonstrates a more sensitive biological interaction of AZ61 material with RAW 264.7^{LPS} when compared to Mg, manifesting as changes in the surface with more protein recruitment and destabilized Ca/P layers. Although the Mg material appears to strongly modulate the fluid compartment by increases in pH and RNS, the changes do not appear on the surface of the degrading material as a change in Ca/P ratio. When taken with the higher amount of CC3 staining, this suggests that the degradation environment produced by Mg to a greater extent overwhelms the ability of RAW 264.7^{LPS} to modulate precise surface chemistry changes, but still experiences local corrosion attack to a higher degree than the unstimulated state. It is possible that AZ61 succumbs to the proinflammatory RAW 264.7^{LPS} cells' ability to regulate the fluid compartment via secretion of ROS-RNS, regulation of pH, or

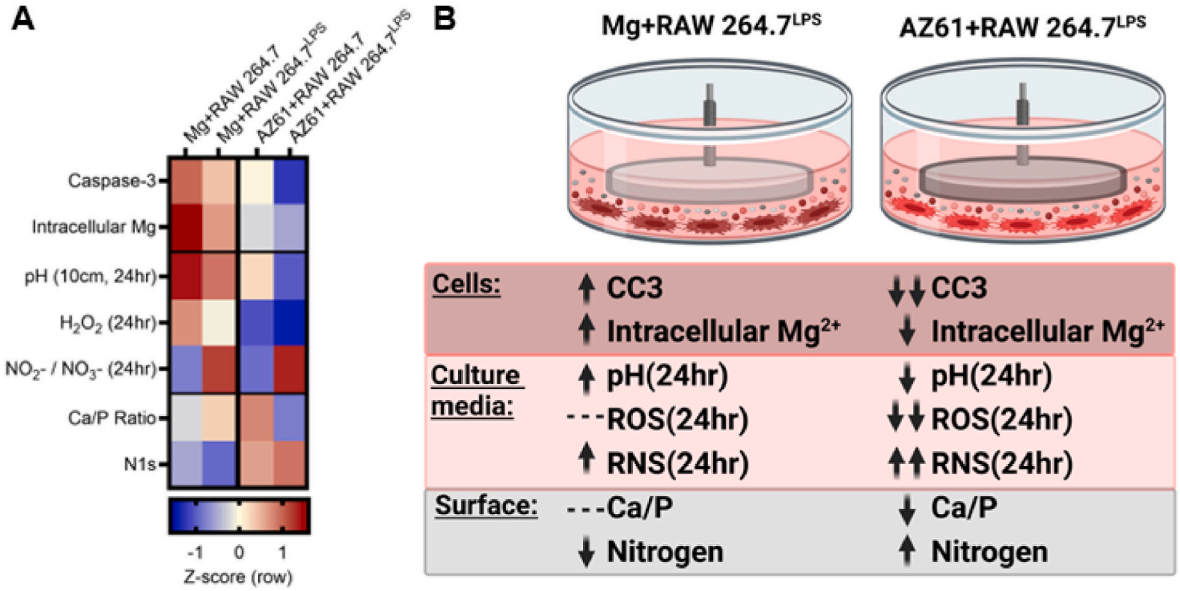

Fig. 6. The relationship between RAW 264.7^{LPS} biological response and surface modulation of degrading Mg and AZ61 metal materials. A, Z-score heat map visualization and **B,** Schematic illustration of cellular, fluidic and material surface changes observed for Mg and AZ61 in a pro-inflammatory microenvironment.

some combination thereof.

4.5. Study limitations

Although our findings clearly demonstrate an influence of degradable Mg based materials on ROS-RNS balance in LPS stimulated conditions with distinct changes in the surface and bulk films of Mg and AZ61, decoupling the contribution of RNS or ROS to these changes would remain challenging in this system. Future studies should evaluate RNS species such as peroxynitrite and NO, in conjunction with ROS species like superoxide in more simplified systems to evaluate the role of these molecules in Mg degradation. Additionally, determining if the changes in the AZ61 and Mg surface film Ca/P presentation, caused by inflammatory stimulation, would manifest as significant alterations in the corrosion rate would require extensive experimental design. For example, discs were only incubated for 24 and 72 h, primarily due to the hyperproliferative capacity of RAW264.7 cells. Future studies should use primary cell cultures that have a slower proliferative rate to accommodate long term assessment of the observations depicted in this study. Our study evaluated ROS-RNS concentration in the total solution, however concentrations near the material-solution-cell interface could be different. Mg concentration and pH gradients caused by local Mg degradation have been demonstrated near Mg discs in solution [59,60] and our viability data shows a differential toxicity environment near and far away from the degrading discs. More studies are needed to describe this critical zone that expressed enhanced proinflammatory macrophages in direct communication with degrading Mg materials.

5. Conclusions

In this study, we show that.

1. Proinflammatory iNOS and F4/80+ expressing macrophages were present at 24hrs near the interface of Mg and AZ31 when implanted subcutaneously in vivo
2. Proinflammatory RAW 264.7^{LPS} macrophages caused more localized corrosion attack when incubated with suspended Mg discs
3. When RAW 264.7^{LPS} macrophages were incubated with suspended AZ61 discs, the bulk corrosion products presented morphological and elemental differences, and the surface Ca/P ratio was decreased
4. The proinflammatory RAW 264.7^{LPS} macrophages had increased viability when incubated with degrading Mg, and the effect was spatially dependent.
5. RAW 264.7^{LPS} macrophages caused an increase in extracellular ROS-RNS secretion, and a decrease in extracellular peroxidase activity in the absence of Mg and AZ61.
6. Actively degrading Mg and AZ61 regulated ROS-RNS balance independent of physiological antioxidant mechanisms in pro-inflammatory RAW 264.7^{LPS} macrophage environment.

Ethics approval and consent to participate

Animal experiments were used in this research study. The protocol was approved by the Michigan Technological University Institutional Animal Care and Use Committee (IACUC) and in accordance with the guidelines set by the Panel on Euthanasia of the American Veterinary Medical Association.

Funding

This work was partially funded by Michigan Tech Research Excellence Fund, National Institutes of Health [grant number R15GM135875 (B.P.L.)]; and the National Science Foundation [grant number DMR 2001076 (B.P.L.)], ZA was partially funded by Michigan Tech Undergraduate Research Internship Program.

CRediT authorship contribution statement

Maria P. Kwesiga: Conceptualization, Methodology, Supervision, Writing – original draft, Investigation, Formal analysis. **Amani A. Gillette:** Methodology, Formal analysis. **Fatemeh Razaviamri:** Investigation, Formal analysis. **Margaret E. Plank:** Investigation, Formal analysis. **Alexia L. Canull:** Investigation, Formal analysis. **Zachary Alesch:** Investigation, Formal analysis. **Weilue He:** Writing – review & editing. **Bruce P. Lee:** Writing – review & editing, Resources. **Roger J. Guillory:** Conceptualization, Methodology, Supervision, Writing – original draft, Investigation, Formal analysis, Resources.

Declaration of competing interest

The authors have no conflicts of interest.

Acknowledgements

We would like to thank Dr. Malgorzata Sikora-Jasinska for assisting with device fabrication and SEM imaging and Dr. Smitha Rao for use of microscopy facilities. Parts of this study were completed using Michigan Technological University's Applied Chemical and Morphological Analysis Laboratory and College of Forest Resources and Environmental Science (ICP-OES analysis). The graphical abstract and schematic figures were created with BioRender.com.

Appendix A. Supplementary data

Supplementary data to this article can be found online at https://doi.org/10.1016/j.bioactmat.2022.10.017.

References

[1] M.A. Khan, M.J. Hashim, H. Mustafa, M.Y. Baniyas, S.K.B.M. Al Suwaidi, R. AlKatheeri, F.M.K. Alblooshi, M.E.A.H. Almatrooshi, M.E.H. Alzaabi, R.S. Al Darmaki, S.N.A.H. Lootah, Global epidemiology of ischemic heart disease: results from the global burden of disease study, Cureus 12 (7) (2020) e9349-e9349.
[2] L. Mauri, D.J. Kereiakes, R.W. Yeh, P. Driscoll-Shempp, D.E. Cutlip, P.G. Steg, S.-L. T. Normand, E. Braunwald, S.D. Wiviott, D.J. Cohen, D.R. Holmes, M.W. Krucoff, J. Hermiller, H.L. Dauerman, D.I. Simon, D.E. Kandzari, K.N. Garratt, D.P. Lee, T. K. Pow, P. Ver Lee, M.J. Rinaldi, J.M. Massaro, Twelve or 30 Months of dual antiplatelet therapy after drug-eluting stents, N. Engl. J. Med. 371 (23) (2014) 2155–2166.
[3] S. Elmariah, L. Mauri, G. Doros, B.Z. Galper, K.E. O'Neill, P.G. Steg, D.J. Kereiakes, R.W. Yeh, Extended duration dual antiplatelet therapy and mortality: a systematic review and meta-analysis, Lancet 385 (9970) (2015) 792–798.
[4] A.E. Denktas, C. Grines, Chapter 19 - percutaneous coronary intervention, in: G. N. Levine (Ed.), Cardiology Secrets, Fifth Edition, Elsevier, 2018, pp. 172–182.
[5] J.W. Jukema, J.J.W. Verschuren, T.A.N. Ahmed, P.H.A. Quax, Restenosis after PCI. Part 1: pathophysiology and risk factors, Nat. Rev. Cardiol. 9 (1) (2012) 53–62.
[6] A.A. Oliver, M. Sikora-Jasinska, A.G. Demir, R.J. Guillory, Recent advances and directions in the development of bioresorbable metallic cardiovascular stents: insights from recent human and in vivo studies, Acta Biomater. 127 (2021) 1–23.
[7] J.-L. Wang, J.-K. Xu, C. Hopkins, D.H.-K. Chow, L. Qin, Biodegradable magnesium-based implants in orthopedics—a general review and perspectives, Adv. Sci. 7 (8) (2020), 1902443.
[8] L.F. Abu-Niaaj, G. Harris, S. Pixley, The role of magnesium biodegradable material in peripheral nerve repair, Faseb. J. 34 (S1) (2020), 1-1.
[9] H. Helmholz, O. Will, T. Penate-Medina, J. Humbert, T. Damm, B. Luthringer-Feyerabend, R. Willumeit-Römer, C.C. Glüer, O. Penate-Medina, Tissue responses after implantation of biodegradable Mg alloys evaluated by multimodality 3D micro-bioimaging in vivo, J. Biomed. Mater. Res. 109 (8) (2021) 1521–1529.
[10] L. Jin, C. Chen, G. Jia, Y. Li, J. Zhang, H. Huang, B. Kang, G. Yuan, H. Zeng, T. Chen, The bioeffects of degradable products derived from a biodegradable Mg-based alloy in macrophages via heterophagy, Acta Biomater. 106 (2020) 428–438.
[11] J. Wang, F. Witte, T. Xi, Y. Zheng, K. Yang, Y. Yang, D. Zhao, J. Meng, Y. Li, W. Li, Recommendation for modifying current cytotoxicity testing standards for biodegradable magnesium-based materials, Acta Biomater. 21 (2015) 237–249.
[12] J. Wang, L. Liu, Y. Wu, M.F. Maitz, Z. Wang, Y. Koo, A. Zhao, J. Sankar, D. Kong, N. Huang, Ex vivo blood vessel bioreactor for analysis of the biodegradation of magnesium stent models with and without vessel wall integration, Acta Biomater. 50 (2017) 546–555.
[13] D. Persaud-Sharma, A. McGoron, Biodegradable magnesium alloys: a review of material development and applications, J. Biomim. Biomater. Tissue Eng. 12 (2012) 25–39.

[14] R. Erbel, C. Di Mario, J. Bartunek, J. Bonnier, B. de Bruyne, F.R. Eberli, P. Erne, M. Haude, B. Heublein, M. Horrigan, Temporary scaffolding of coronary arteries with bioabsorbable magnesium stents: a prospective, non-randomised multicentre trial, Lancet 369 (9576) (2007) 1869–1875.
[15] M. Haude, R. Erbel, P. Erne, S. Verheye, H. Degen, D. Böse, P. Vermeersch, I. Wijnbergen, N. Weissman, F. Prati, Safety and performance of the drug-eluting absorbable metal scaffold (DREAMS) in patients with de-novo coronary lesions: 12 month results of the prospective, multicentre, first-in-man BIOSOLVE-I trial, Lancet 381 (9869) (2013) 836–844.
[16] M. Haude, H. Ince, A. Abizaid, R. Toelg, P.A. Lemos, C. von Birgelen, E. H. Christiansen, W. Wijns, F.-J. Neumann, C. Kaiser, Safety and performance of the second-generation drug-eluting absorbable metal scaffold in patients with de-novo coronary artery lesions (BIOSOLVE-II): 6 month results of a prospective, multicentre, non-randomised, first-in-man trial, Lancet 387 (10013) (2016) 31–39.
[17] S. Brugaletta, A. Cequier, F. Alfonso, A. Iñiguez, S. Romaní, A. Serra, P. Salinas, J. Goicolea, P. Bordes, B.G. del Blanco, R. Hernández-Antolín, A. Pernigotti, J. Gómez-Lara, M. Sabaté, MAGnesium-based bioresorbable scaffold and vasomotor function in patients with acute ST segment elevation myocardial infarction: the MAGSTEMI trial: rationale and design, Cathet. Cardiovasc. Interv. 93 (1) (2019) 64–70.
[18] J.M. Hare, Nitroso-redox balance in the cardiovascular system, N. Engl. J. Med. 351 (20) (2004) 2112–2114.
[19] W. He, M.P. Kwesiga, E. Gebreyesus, S. Liu, Nitric Oxide and Oxidative Stress-Mediated Cardiovascular Functionality: from Molecular Mechanism to Cardiovascular Disease, Vascular Biology-Selection of Mechanisms and Clinical Applications, IntechOpen, 2019.
[20] H. Ischiropoulos, L. Zhu, J.S. Beckman, Peroxynitrite formation from macrophage-derived nitric oxide, Arch. Biochem. Biophys. 298 (2) (1992) 446–451.
[21] D.T. Sawyer, J.S. Valentine, How super is superoxide? Acc. Chem. Res. 14 (12) (1981) 393–400.
[22] P. Pacher, J.S. Beckman, L. Liaudet, Nitric oxide and peroxynitrite in health and disease, Physiol. Rev. 87 (1) (2007) 315–424.
[23] L. Jin, C. Chen, Y. Li, F. Yuan, R. Gong, J. Wu, H. Zhang, B. Kang, G. Yuan, H. Zeng, A biodegradable Mg-based alloy inhibited the inflammatory response of THP-1 cell-derived macrophages through the TRPM7–PI3K–AKT1 signaling axis, Front. Immunol. 10 (2019) 2798.
[24] J. Zhang, S. Hiromoto, T. Yamazaki, J. Niu, H. Huang, G. Jia, H. Li, W. Ding, G. Yuan, Effect of macrophages on in vitro corrosion behavior of magnesium alloy, J. Biomed. Mater. Res., Part A 104 (10) (2016) 2476–2487.
[25] G. Ambrozova, M. Pekarova, A. Lojek, The effect of lipid peroxidation products on reactive oxygen species formation and nitric oxide production in lipopolysaccharide-stimulated RAW 264.7 macrophages, Toxicol. Vitro 25 (1) (2011) 145–152.
[26] W.-K. Ko, S.-H. Lee, S.J. Kim, M.-J. Jo, H. Kumar, I.-B. Han, S. Sohn, Anti-inflammatory effects of ursodeoxycholic acid by lipopolysaccharide-stimulated inflammatory responses in RAW 264.7 macrophages, PLoS One 12 (6) (2017), e0180673.
[27] C. Li, C. Guo, V. Fitzpatrick, A. Ibrahim, M.J. Zwierstra, P. Hanna, A. Lechtig, A. Nazarian, S.J. Lin, D.L. Kaplan, Design of biodegradable, implantable devices towards clinical translation, Nat. Rev. Mater. 5 (1) (2020) 61–81.
[28] C. McQuin, A. Goodman, V. Chernyshev, L. Kamentsky, B.A. Cimini, K.W. Karhohs, M. Doan, L. Ding, S.M. Rafelski, D. Thirstrup, CellProfiler 3.0: next-generation image processing for biology, PLoS Biol. 16 (7) (2018), e2005970.
[29] A.J. Walsh, M.C. Skala, Optical metabolic imaging quantifies heterogeneous cell populations, Biomed. Opt Express 6 (2) (2015) 559–573.
[30] W. Pan, M.M. Wall, Small-sample adjustments in using the sandwich variance estimator in generalized estimating equations, Stat. Med. 21 (10) (2002) 1429–1441.
[31] H. Akaike, A new look at the statistical model identification, IEEE Trans. Automat. Control 19 (6) (1974) 716–723.
[32] C. Haan, I. Behrmann, A cost effective non-commercial ECL-solution for Western blot detections yielding strong signals and low background, J. Immunol. Methods 318 (1) (2007) 11–19.
[33] P. Khan, D. Idrees, M.A. Moxley, J.A. Corbett, F. Ahmad, G. von Figura, W.S. Sly, A. Waheed, M. Hassan, Luminol-based chemiluminescent signals: clinical and non-clinical application and future uses, Appl. Biochem. Biotechnol. 173 (2) (2014) 333–355.
[34] M.M. Bradford, A rapid and sensitive method for the quantitation of microgram quantities of protein utilizing the principle of protein-dye binding, Anal. Biochem. 72 (1–2) (1976) 248–254.
[35] J. Sun, X. Zhang, M. Broderick, H. Fein, Measurement of nitric oxide production in biological systems by using Griess reaction assay, Sensors 3 (8) (2003) 276–284.
[36] F. Aktan, iNOS-mediated nitric oxide production and its regulation, Life Sci. 75 (6) (2004) 639–653.
[37] C.J. Lowenstein, E. Padalko, iNOS (NOS2) at a glance, J. Cell Sci. 117 (14) (2004) 2865–2867.
[38] A. dos Anjos Cassado, F4/80 as a major macrophage marker: the case of the peritoneum and spleen, Macrophages (2017) 161–179.
[39] Zainuddin Bin Sajuri, Yukio Miyashita, Yasunobu Hosokai, Yoshiharu Mutoh, Effects of Mn content and texture on fatigue properties of as-cast and extruded AZ61 magnesium alloys, Int. J. Mech. Sci. 48 (2) (2005) 198–209.
[40] J.D. Andrade, X-Ray photoelectron spectroscopy (XPS), in: J.D. Andrade (Ed.), Surface and Interfacial Aspects of Biomedical Polymers: Volume 1 Surface Chemistry and Physics, Springer US, Boston, MA, 1985, pp. 105–195.
[41] D. Tie, F. Feyerabend, N. Hort, R. Willumeit, D. Hoeche, XPS studies of magnesium surfaces after exposure to Dulbecco's modified eagle medium, Hank's buffered salt solution, and simulated body fluid, Adv. Eng. Mater. 12 (12) (2010) B699–B704.
[42] J. Arthur, The glutathione peroxidases, Cellular and Molecular Life Sciences CMLS 57 (13) (2001) 1825–1835.
[43] M. Costantino, A. Schuster, H. Helmholz, A. Meyer-Rachner, R. Willumeit-Römer, B. Luthringer-Feyerabend, Inflammatory response to magnesium-based biodegradable implant materials, Acta Biomater. 101 (2020) 598–608.
[44] Q. Peng, K. Li, Z. Han, E. Wang, Z. Xu, R. Liu, Y. Tian, Degradable magnesium-based implant materials with anti-inflammatory activity, J. Biomed. Mater. Res. 101 (7) (2013) 1898–1906.
[45] X. Liu, W. Li, Y. Cheng, Y. Zheng, The effect of simulated inflammatory conditions on the corrosion of Mg, Fe and CoCrMo, Mater. Lett. 308 (2022), 131197.
[46] E.K. Brooks, S. Der, M.T. Ehrensberger, Corrosion and mechanical performance of AZ91 exposed to simulated inflammatory conditions, Mater. Sci. Eng. C 60 (2016) 427–436.
[47] J. Gonzalez, R.Q. Hou, E.P. Nidadavolu, R. Willumeit-Römer, F. Feyerabend, Magnesium degradation under physiological conditions–best practice, Bioact. Mater. 3 (2) (2018) 174–185.
[48] V. Wagener, S. Virtanen, Protective layer formation on magnesium in cell culture medium, Mater. Sci. Eng. C 63 (2016) 341–351.
[49] A.G. Porter, R.U. Jänicke, Emerging roles of caspase-3 in apoptosis, Cell Death Differ. 6 (2) (1999) 99–104.
[50] Y. Wen, Q. Liu, J. Wang, Q. Yang, W. Zhao, B. Qiao, Y. Li, D. Jiang, Improving in vitro and in vivo corrosion resistance and biocompatibility of Mg–1Zn–1Sn alloys by microalloying with Sr, Bioact. Mater. 6 (12) (2021) 4654–4669.
[51] D. Dziuba, A. Meyer-Lindenberg, J.M. Seitz, H. Waizy, N. Angrisani, J. Reifenrath, Long-term in vivo degradation behaviour and biocompatibility of the magnesium alloy ZEK100 for use as a biodegradable bone implant, Acta Biomater. 9 (10) (2013) 8548–8560.
[52] N. Zhao, N. Watson, Z. Xu, Y. Chen, J. Waterman, J. Sankar, D. Zhu, In vitro biocompatibility and endothelialization of novel magnesium-rare Earth alloys for improved stent applications, PLoS One 9 (6) (2014), e98674.
[53] T. Liu, L. Zhang, D. Joo, S.-C. Sun, NF-κB signaling in inflammation, Signal Transduct. Targeted Ther. 2 (1) (2017), 17023.
[54] J.L. Luo, H. Kamata, M. Karin, IKK/NF-kappaB signaling: balancing life and death–a new approach to cancer therapy, J. Clin. Investig. 115 (10) (2005) 2625–2632.
[55] K.W. Beyenbach, Transport of magnesium across biological membranes, Magnes. Trace. Elem. 9 (5) (1990) 233–254.
[56] A. Bordbar-Khiabani, B. Yarmand, S. Sharifi-Asl, M. Mozafari, Improved corrosion performance of biodegradable magnesium in simulated inflammatory condition via drug-loaded plasma electrolytic oxidation coatings, Mater. Chem. Phys. 239 (2020), 122003.
[57] S. Wang, S.-J. Zhu, X.-Q. Zhang, J.-A. Li, S.-K. Guan, Effects of degradation products of biomedical magnesium alloys on nitric oxide release from vascular endothelial cells, Med. Gas Res. 9 (3) (2019) 153.
[58] M. Dhruvaraj, Role of peroxidase in clinical assays: a short review, J. Clin. Nutr. 3 (2) (2017) 14.
[59] S.V. Lamaka, J. Gonzalez, D. Mei, F. Feyerabend, R. Willumeit-Römer, M. L. Zheludkevich, Local pH and its evolution near Mg alloy surfaces exposed to simulated body fluids, Adv. Mater. Interfac. 5 (18) (2018), 1800169.
[60] J. Gonzalez, S.V. Lamaka, D. Mei, N. Scharnagl, F. Feyerabend, M.L. Zheludkevich, R. Willumeit-Römer, Mg biodegradation mechanism deduced from the local surface environment under simulated physiological conditions, Adv. Healthcare Mater. 10 (13) (2021), 2100053.